Spherical Parametrization and Remeshing

Emil Praun
University of Utah

Hugues Hoppe
Microsoft Research

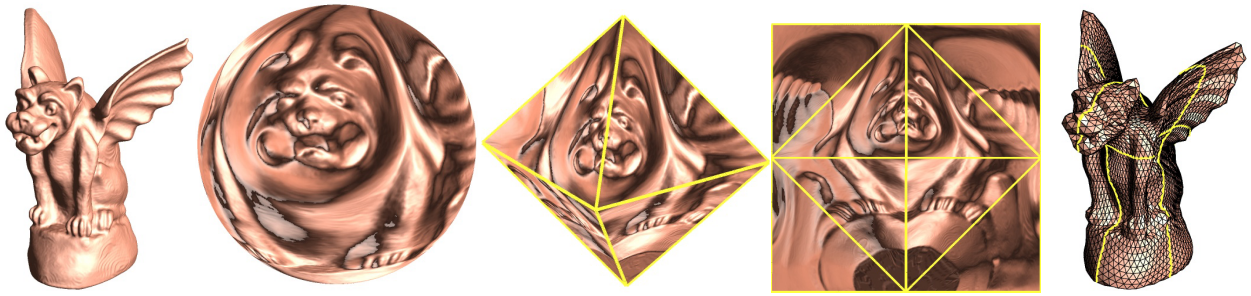

original | spherical parametrization | octahedral parametrization | geometry image (lit) | remeshed geometry

Figure 1: Demonstration of spherical parametrization and subsequent resampling into a geometry image.

Abstract

The traditional approach for parametrizing a surface involves cutting it into charts and mapping these piecewise onto a planar domain. We introduce a robust technique for directly parametrizing a genus-zero surface onto a spherical domain. A key ingredient for making such a parametrization practical is the minimization of a stretch-based measure, to reduce scale-distortion and thereby prevent undersampling. Our second contribution is a scheme for sampling the spherical domain using uniformly subdivided polyhedral domains, namely the tetrahedron, octahedron, and cube. We show that these particular semi-regular samplings can be conveniently represented as completely regular 2D grids, i.e. geometry images. Moreover, these images have simple boundary extension rules that aid many processing operations. Applications include geometry remeshing, level-of-detail, morphing, compression, and smooth surface subdivision.

Keywords: texture mapping, remeshing, geometry images, meshes.

1. Introduction

Surface parametrization. To associate a given surface with a planar domain, the traditional approach is to partition the surface into charts, parametrize these in the plane, and pack them into a **texture atlas**, as shown in the example on the right [e.g. Maillot et al. 1993; Cignoni et al. 1998; Sander et al. 2001; Lévy et al. 2002]. One main drawback of an atlas is the presence of visible seams on the surface. Sheffer and Hart [2002] try to hide these seams in high-curvature regions.

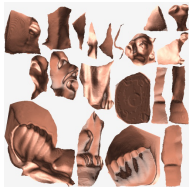

An alternative is **semi-regular remeshing** whereby the connectivity of the surface charts is used to form a domain complex that is then regularly subdivided [e.g. Eck et al. 1995; Lee et al. 1998; Kobbelt et al. 1999; Guskov et al. 2000 ; Lee et al. 2000; Wood et al. 2000]. Because the connectivity of the domain complex itself is irregular, applying a texture image to the surface requires storing a parametrization.

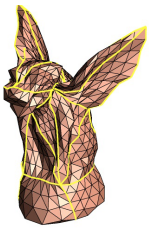

Recently, Gu et al. [2002] introduced **geometry images**, in which geometry is resampled into a completely regular 2D grid. The process involves cutting the surface into a disk using a network of cut paths, and then mapping the boundary of this disk to a square. Both geometry and other signals are stored as 2D grids, with grid samples in implicit correspondence, obviating the need to store a parametrization. Also, the boundary parametrization makes both geometry and textures seamless.

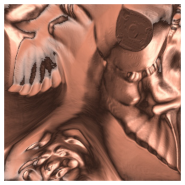

In all three approaches, the surface is first cut into one or more disk-like charts using a network of cut paths, and a parametrization is formed piecewise on each chart. The *a priori* construction of the chart boundaries or cut paths is heuristic, and constrains the quality of the attainable parametrization. In texture atlases, both the number of charts and their surface extents are selected heuristically to minimize parametric distortion onto planar polygons, while also maintaining good packing efficiency. In semi-regular remeshing, surface charts are selected to have low-distortion maps onto regular domain faces, and to have approximately the same size. Finally, in geometry images, the surface is heuristically cut into a disk that hopefully maps well onto a square.

Sorkine et al. [2002] take the interesting approach of parametrizing a chart during its incremental growth, to bound distortion. Thus, the creation of cut paths is guided by the parametrization.

In this paper, we construct for a common class of models a continuous, unconstrained parametrization without any cutting.

Spherical parametrization. Geometric models are often described by closed, genus-zero surfaces, i.e. deformed spheres. For such models, the sphere is the most natural parametrization domain, since it does not require cutting the surface into disk(s). Hence the parametrization process becomes unconstrained. Even though we may subsequently resample the surface signal onto a piecewise continuous domain, these domain boundaries can be determined more conveniently and *a posteriori* on the sphere.

While planar parametrization of mesh charts has been studied extensively, there is relatively less work on parametrizing a mesh as a whole onto a spherical domain, as reviewed in Section 3.1.

Spherical parametrization proves to be challenging in practice, for two reasons. First, for the algorithm to be robust it must prevent parametric "foldovers" and thus guarantee a 1-to-1 spherical map. Second, while all genus-zero surfaces are in essence sphere-shaped, some can be highly deformed, and creating a parametrization that adequately samples all surface regions is difficult.

To address these challenges, our parametrization algorithm borrows techniques from Sander et al. [2001, 2002]. We achieve robustness using a coarse-to-fine optimization strategy, and penalize undersampling using a stretch-based parametrization metric (Section 3). Intuitively, stretch measures how distances in the domain get scaled onto the surface. Large stretch in any direction about a surface point implies that the reconstruction of the surface signal from a domain-uniform sampling will lose high-frequency surface detail.

Once a spherical parametrization is obtained, a number of applications can operate directly on the sphere domain, including shape analysis using spherical harmonics [Funkhouser et al. 2003; Quicken et al. 2000], compression using spherical wavelets [Schröder and Sweldens 1995], and mesh morphing [Alexa 2002].

Spherical remeshing. Many techniques rely on sampled representations, and unfortunately, the only truly uniform samplings of the sphere are given by the vertices of the 5 Platonic solids (icosahedron being the most complex with 20 vertices).

In computer graphics, spherical functions such as environment and visibility maps are often represented using cube maps [Greene 1986]. While this cube projection is hardware-efficient, it creates a rather non-uniform spherical sampling (with stretch varying by a factor of 3). Unlike in environment maps, spherical directions have no special meaning for surface parametrizations. Thus we are free to construct maps that distribute samples more uniformly.

As a sampling pattern, we use the vertices of uniformly subdivided regular polyhedra, namely the tetrahedron, octahedron, and cube. We explore maps with minimal stretch from these domains to the sphere (Section 4.2).

Geometry images. The semi-regular samples that we construct over the polyhedral domains can in fact be cut and unfolded such that they correspond 1-to-1 with a regular 2D grid (Section 4.1). We use these unfoldings to resample our spherical parametrizations into geometry images (see Figure 1).

The simple 2D grid structure of geometry images is ideally suited for many processing operations. For instance, they can be rendered by traversing the grids sequentially, without expensive memory-gather operations (such as vertex index dereferencing or random-access texture filtering). Geometry images also facilitate compression and level-of-detail control.

The geometry images introduced by Gu et al. [2002] support surfaces of arbitrary genus by allowing an arbitrary surface cut. However, the cut topology must be stored explicitly for lossy decompression, and it constrains level-of-detail mip-mapping.

In contrast, our construction is specialized to genus-zero surfaces, and the topology of our polyhedral cuts is fixed and simple. The cuts give rise to symmetry rules at the image boundaries, which enable morphing, better level-of-detail control, more effective compression, and the creation of smooth surfaces.

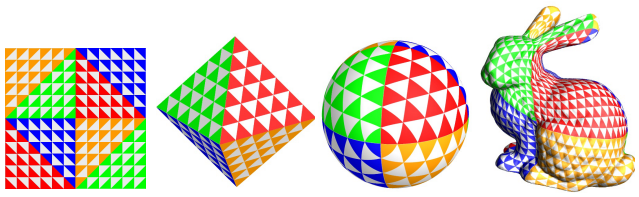

image I domain D sphere S surface mesh M

Figure 2: Overview of the parametrization process.

2. Approach overview

Given a surface mesh M, our goal is to create a geometry image I that approximates it. We first create a spherical parametrization of the surface ($S \rightarrow M$). Next, we similarly create a spherical parametrization ($S \rightarrow D$) of a domain polyhedron D, chosen to be a tetrahedron, an octahedron, or a cube. Finally, we unfold the domain into the image ($D \rightarrow I$). All these maps are invertible, and their composition provides a map $I \rightarrow D \rightarrow S \rightarrow M$ (see Figure 2).

For remeshing, we uniformly sample the domain polyhedron at the vertices of a regular n-tessellation (n+1 vertices on each domain edge). As explained in Section 4.1, the unfolding ($I \leftrightarrow D$) is not an isometry and we are not concerned with its metric distortion – it is a convenient scheme for associating the domain samples 1-to-1 with the 2D grid samples of the image.

To avoid undersampling of the surface mesh, we seek to minimize the stretch of the map $D \rightarrow M$. We do this by minimizing stretch on the two maps $D \rightarrow S$ and $S \rightarrow M$. Both maps involve the computation of a spherical parametrization, as discussed next.

3. Spherical parametrization

Given a triangle mesh M, the problem of spherical parametrization is to form a continuous invertible map $\phi : S \rightarrow M$ from the unit sphere to the mesh. The map is specified by assigning each mesh vertex v a parametrization $\phi^{-1}(v) \in S$. Each mesh edge is mapped to a *great circle arc*, and each mesh triangle is mapped to a *spherical triangle* bounded by these arcs.

3.1 Previous work

Kent et al. [1992] propose several spherical parametrization schemes. For general shapes, they simulate a balloon inflation process, but are not able to guarantee a 1-to-1 map.

Alexa [2002] uses a spring-like relaxation process. The relaxation solutions may collapse to a point, or experience foldovers, depending on the starting state. He demonstrates several heuristics that help the solution converge to valid maps.

Grimm [2002] partitions the surface into 6 charts, and maps these to faces of a cube, and from there to a sphere. Schemes based on a priori chart partitions constrain the spherical parametrization.

Haker et al. [2000] find conformal approximations of meshes over the sphere. Conceptually, they remove a single point from the surface, harmonically map the remaining surface onto an infinite plane, and finally map that infinite plane onto the sphere using stereographic projection. Both maps are conformal for smooth surfaces. Unfortunately, many maps that are bijective and conformal for smooth surfaces do not guarantee an embedding when applied to piecewise-linear surfaces (meshes), and sometimes produce triangle flips, as in Eck et al. [1995]. For instance, stereographic projection can flip thin obtuse triangles. Another concern with conformal-like maps is scale distortion (Figure 11).

Sheffer et al. [2003] find the angles of a spherical embedding as a constrained nonlinear system, and show results for simple meshes.

Gotsman et al. [2003] show a nice relationship between spectral graph theory and spherical parametrization, and embed simple meshes on the sphere by solving a quadratic system.

Quicken et al. [2000] parametrize the surface of a voxel volume onto a sphere. Their nonlinear objective functional exploits the uniform quadrilateral structure of the voxel surface; it seeks to equalize areas and preserve right-angles of surface elements. Their scheme is not applicable to general triangle meshes.

These prior schemes cannot parametrize a complex mesh robustly and with the low scale-distortion necessary for good remeshing.

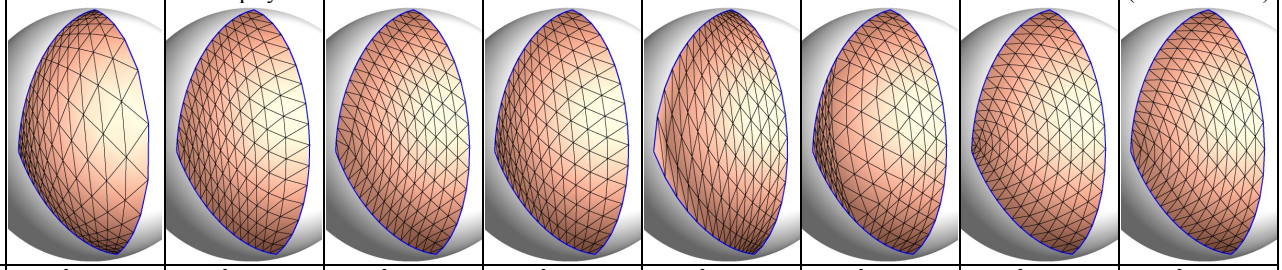

$D\rightarrow S$	L^2=0.31	L^2=0.67	L^2=0.75	L^2=0.70	L^2=0.40	L^2=0.71	L^2=0.85	(L^2=0.80)
$S\rightarrow D$	L^2=0.23	L^2=0.55	L^2=0.73	L^2=0.45	L^2=0.42	L^2=0.32	L^2<0.01	(L^2=0.75)

Figure 3: Comparison of spherical triangle maps for a large spherical triangle, and computed stretch efficiencies in both map directions. (The black curves show a uniform tessellation of the planar triangle in domain D mapped onto the sphere S.)

3.2 Spherical triangle map

To form a continuous parametrization ϕ, we must define the map within each triangle interior. Let the points $\{A,B,C\}$ on the sphere be the parametrization of the vertices of a mesh triangle $\{A'=\phi(A), B'=\phi(B), C'=\phi(C)\}$. Given a point $P'= \alpha A'+\beta B'+\gamma C'$ with barycentric coordinates $\alpha+\beta+\gamma=1$ within the mesh triangle, we must define its parametrization $P=\phi^{-1}(P')$. Any such mapping must have distortion since the spherical triangle is not developable. We have explored several mappings (Figure 3):

Gnomonic: It is simply spherical projection about the sphere center O. That is, $P = (\alpha A+\beta B+\gamma C) / \|\alpha A+\beta B+\gamma C\|$. The inverse is easily computable as spherical projection back onto the triangle.

2-slerp-symmetrized: Spherical linear interpolation slerp$(A,B,\alpha) = P$ finds P such that arclen(A,P) / arclen$(P,B) = \alpha / (1-\alpha)$. A possible triangle interpolation scheme is to perform two consecutive slerps: 2-slerp$(A,B,C,\alpha,\beta,1-\alpha-\beta)$ = slerp(slerp$(A, B, \beta/(\alpha+\beta))$, C, $1-\alpha-\beta)$. Unfortunately, this definition is not symmetric since 2-slerp$(A,B,C,\alpha,\beta,\gamma) \neq$ 2-slerp$(B,C,A,\beta,\gamma,\alpha)$. However, symmetry can be obtained by averaging three 2-slerp's and renormalizing:

$$\text{2-slerp-sym}(A,B,C,\alpha,\beta,\gamma) = \text{normalize}[\alpha\ \text{2-slerp}(A,B,C,\alpha,\beta,\gamma) + \beta\ \text{2-slerp}(B,C,A,\beta,\gamma,\alpha) + \gamma\ \text{2-slerp}(C,A,B,\gamma,\alpha,\beta)\ ].$$

Arvo◦Turk^{-1}-symmetrized: Arvo [1995] presents an area-uniform map from a square to a spherical triangle. Turk [1990] presents an area-uniform map from a square to a triangle. The composition of the two maps, Arvo◦Turk^{-1}, is an area-uniform map from a triangle to a spherical triangle. Unfortunately, the map is not symmetric, so like 2-slerp it requires symmetrization. This map is fairly expensive to compute since it involves several trigonometric evaluations.

Buss-Fillmore [2001]: They define barycentric combinations of spherical points $A_1,\ldots,A_k$ as least-squares minimizations of weighted geodesic distances. Even for k=3, the minimization problem requires an iterative solution, but it converges quickly. The scheme has the property that if one takes the exponential map around the resulting point P (mapping each A_i to a point B_i in the plane tangent to the sphere at P such that $\|PB_i\|$ = arclen(PA_i) and P,A_i,B_i,O are coplanar), then P is the convex combination of the points B_i with the provided initial weights. Consequently, the spherical triangle map is easy to invert.

Spherical area map: In this map, we obtain P such that the barycentric coordinates (α,β,γ) match the ratios of spherical areas of the 3 introduced spherical sub-triangles (P,B,C), (A,P,C), and (A,B,P). We have not been able to locate a reference to this map in the literature. To obtain P, we first find the points D,E,F such that area$(D,B,C) = \alpha*$area(A,B,C), area$(A,\mathrm{E},C) = \beta*$area$(A,B,C)$, and area$(A,B,F) = \gamma*$area$(A,B,C)$. Todhunter and Leathem [1949] prove that the locus of points that together with an arc XY form spherical triangles of a given (constant) area is a small circle passing through X^* and Y^*, the antipodes of X and Y. Therefore, P is found at the intersection of the small circles supporting (D,B^*,C^*), (A^*,E,C^*), and (A^*,B^*,F). The inverse map is easy to compute, since it simply involves computing the ratios of the areas of the spherical sub-triangles.

Recursive subdivision: Both the triangle and spherical triangle are recursively split using regular 1-to-4 subdivision [Schröder and Sweldens 1995], while tracking the location of the desired barycentric coordinates. Since the map is not smooth, neither the forward nor the inverse map has a closed-form expression.

Stretch optimization: For comparison, we also consider the result of finely subdividing the triangle and optimizing stretch in either map direction (as described in Sections 3.4-3.5).

All these maps converge to affine maps as the spherical triangle becomes small, i.e. planar. We next analyze these maps with respect to a number of desirable properties (Table 1): *continuity* at boundaries (across arbitrary adjacent triangles), *arc-length* parametrization of boundary edges, *smoothness* (the map should be differentiable), closed-form (*analytic*) expressions for both the spherical map and its inverse, and distortion minimization (as measured using the *stretch* metric).

In conclusion, no map exhibits all the desired properties. Some maps have better stretch behavior, which is important for parametrizing coarse meshes. However, these maps are more expensive to compute, and behave much like the inexpensive gnomonic map for the small triangles in fine meshes. For performance, we have chosen to use the gnomonic map for the coarse-to-fine optimization of $S\rightarrow M$ (Section 3.5). We had hoped that the good stretch behavior of the Arvo◦Turk^{-1}-symmetrized map would help accelerate the coarse-to-fine optimization process, but our experiments indicate that the overall compute-time convergence rate instead slows. In Section 4.2, we also experiment with all these spherical triangle maps to parametrize the large domain faces in $D\rightarrow S$.

Triangle map	Boundaries		Smooth interior	Analytic		Stretch	
	C^0	arc-len.		$D\rightarrow S$	$S\rightarrow D$	$D\rightarrow S$	$S\rightarrow D$
Gnomonic	yes	**no**	yes	yes	yes	poor	poor
2-slerp-sym.	yes	yes	yes	yes	**no**	ok	ok
Arvo◦Turk^{-1}	yes	**no**	yes	yes	**no**	good	good
Buss-Fillmore	yes	yes	yes	**no**	yes	good	poor
Area	**no**	**no**	yes	yes	yes	poor	poor
Subdivision	yes	yes	**no**	**no**	**no**	good	poor
Stretch optim.	**no**	**no**	visually	**no**	**no**	best	best

Table 1: Desirable properties of a spherical triangle map.

3.3 Review of planar-domain stretch metric

Sander et al. [2001] show that undersampling is directly related to the *stretch* of a parametrization. They consider the case of a parametrization $\phi : D \rightarrow M : (s,t) \in R^2 \rightarrow (x,y,z) \in R^3$, where D is a *planar* domain. At any point (s,t), the singular values Γ and γ of the 3x2 Jacobian matrix $J_\phi = [\ d\phi/ds\ \ d\phi/dt\ ]$ represent the largest and smallest lengths obtained when mapping unit-length vectors from the domain D to the surface S, i.e. the largest and smallest local stretch. They derive two scalar norms corresponding to rms (L^2) and worst-case (L^∞) stretch over all directions in the domain:

$$L^2(s,t) = \sqrt{\tfrac{1}{2}\left(\Gamma^2 + \gamma^2\right)} \quad \text{and} \quad L^\infty(s,t) = \Gamma \ .$$

The L^2-stretch norm is L^2-integrated over the surface M to obtain the stretch metric

$$L^2(M) = \sqrt{\frac{1}{A_M} \iint_{(s,t)\in D} \left(L^2(s,t)\right)^2 \, dA_M(s,t)} \ ,$$

where $dA_M(s,t) = \gamma\,\Gamma\,ds\,dt$ is the differential surface area.

For the case of a triangle mesh, ϕ is piecewise linear and its Jacobian J_ϕ is constant over each triangle. Thus, the integrated metric can be rewritten as a finite sum.

The L^2 *stretch efficiency* is defined as $(A_M / A_D)\,(1/L^2(M)^2)$ where A_M and A_D are the areas of the surface and domain respectively. The stretch efficiency has an upper bound of 1.

3.4 Spherical-domain stretch metric

We extend the definition of stretch to consider a spherical parametrization $\phi : S \rightarrow M : \hat{v} \in S \rightarrow (x,y,z) \in R^3$.

We analyze the map piecewise on each spherical triangle. Let (s,t) be a local orthonormal coordinate frame on a triangle T of M. Because the spherical triangle is non-planar, we find it more convenient to analyze the inverse map $\phi^{-1}(s,t)$ from triangle T back to the sphere. Let $J_{\phi^{-1}}$ be the Jacobian of this inverse map. Around any point $\phi(P)$ inside T, $J_{\phi^{-1}}$ provides a local linear approximation for ϕ^{-1}. Consequently, distances around P get stretched through map ϕ by a factor between $1/\gamma$ and $1/\Gamma$ (with Γ and γ the singular values of $J_{\phi^{-1}}$). Thus, the stretch over the triangle T is

$$L^2(T) = \sqrt{\frac{1}{A_{M_T}} \iint_{(s,t)\in T} \left(\frac{1}{\gamma^2} + \frac{1}{\Gamma^2}\right) dA_{M_T}(s,t)} \ ,$$

where $dA_{M_T}(s,t) = ds\,dt$ is the differential mesh triangle area.

When $\Gamma >> \gamma$, minimizing stretch alone produces oversampling along one direction. Since the parametrization is not well constrained along that direction, the iso-parameter lines become "bunched-up" and wavy (see Figure 11). To avoid this artifact, we add a small regularization term, $\varepsilon(A_M/4\pi)^{p/2+1}(\Gamma)^p$, that penalizes *inverse stretch*. We have found that ε=0.0001 and p=6 work well for all our models. Unlike a conformal energy term, inverse stretch only contributes in regions of oversampling.

Since $J_{\phi^{-1}}$ and therefore Γ and γ are not constant over T, we have to resort to numerical integration. We subdivide each spherical triangle such that the resulting pieces are sufficiently planar (i.e. the length of the longest edge is bounded by a threshold). For each resulting spherical sub-triangle, we can directly point-sample the Jacobian $J_{\phi^{-1}}$ by evaluating the derivatives of the spherical triangle map. Derivative computations are fairly expensive though. Instead, we have found it more efficient to numerically compute $J_{\phi^{-1}}$ by evaluating stretch using the planar triangle spanning its vertices.

However, this planar approximation to computing stretch can grossly underestimate stretch for spherical triangles with bad aspect ratio, regardless of their size. Specifically, as a thin "cap" spherical triangle (with one angle close to 180°) approaches degeneracy, its analytic stretch becomes infinite. In contrast, the stretch measured using the planar approximation approaches a finite constant, since the planar triangle just rotates its plane closer to the sphere origin while maintaining a bounded aspect ratio. In practice, the problem reveals itself during stretch optimization as an "accordion effect".

Our solution is to split each spherical triangle using the perpendicular to the longest edge, prior to subdividing it for numerical integration. This split has the effect of replacing all "cap" triangles with two "needle" triangles (with two angles close to 90°). A needle triangle does not suffer from the same inaccuracy since its shortest planar edge shrinks along with its spherical counterpart.

3.5 Spherical parametrization algorithm

Coarse-to-fine strategy. Minimizing the stretch norm is a nonlinear optimization, and we approach this problem using a coarse-to-fine multiresolution strategy as in Hormann et al. [1999] and Sander et al. [2002]. We simplify the surface mesh M to a tetrahedron while creating a progressive mesh [Hoppe 1996], favoring triangles with good aspect ratios. After mapping the base tetrahedron to the sphere, we traverse the progressive mesh sequence, inserting vertices on the sphere while maintaining an embedding and minimizing the stretch metric. Figure 4 shows some example results.

Vertex insertion. Each vertex split in the progressive mesh specifies a ring of vertices that will be the neighbors of the new vertex. This vertex ring forms a spherical polygon. The *kernel* of this spherical polygon is defined as the intersection of the open hemispheres defined by the polygon edges. To maintain an embedding (i.e. avoid flipped or degenerate triangles), we place the new vertex inside this kernel. Note that if the mapping is an embedding prior to the insertion, the kernel cannot be empty.

Vertex optimization. After inserting a new vertex, we optimize vertices in the neighborhood one at a time. To optimize one vertex, we minimize the stretch metric summed on its adjacent triangles. We perform a set of great-circle searches in random directions on the sphere, using bracketed parabolic minimization. To prevent flipping, we only consider perturbing the vertex within the kernel of its 1-ring. Note that degenerate triangles are avoided since they have infinite stretch energy.

Each time the number of vertices has increased by a constant factor (e.g. 2), we sweep through all mesh vertices and optimize each one in turn. More precisely, we place all vertices in a priority queue ordered by the amount of change in their neighborhood. The process stops when the largest change is below a threshold (e.g. 10^{-3}).

Robustness. We can show by induction that our parametrization algorithm always produces an embedding. We start with an embedding (since the base case is simply a tetrahedron), and we note that both types of operations (vertex insertion and vertex optimization) maintain the embedding. The algorithm can only fail due to numerical precision problems, and we have not experienced any such problems. Shapiro and Tal [1998] use a similar coarse-to-fine refinement strategy to robustly map a mesh onto a convex polyhedron, which could then be projected to a sphere.

Convergence. As in most nonlinear problems, our minimization algorithm is not guaranteed to find a global minimum. The vertex optimizations only decrease the stretch energy functional, and since it is positive, it must converge to a local minimum.

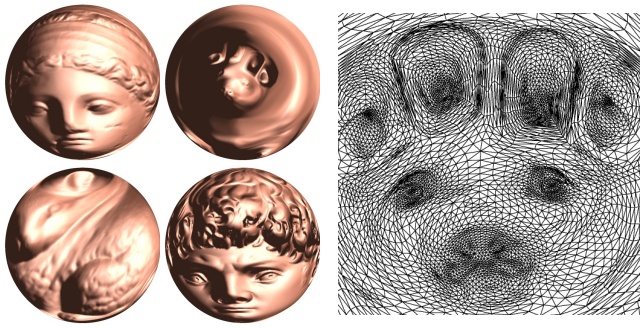

Figure 4: Spherical parametrizations: Venus, cow, bunny, David, and close-up of the cow (showing snout, eyes, ears, and horns).

4. Spherical remeshing

Having parametrized a surface onto the sphere, we now evaluate its signal onto one of three polyhedral domains. First, we show that the samples from a uniform n-tessellation of the three domains can be mapped to geometry images. Second, we present low-stretch parametrizations from the domains to the sphere.

4.1 Domain unfolding ($D \bullet I$)

Our goal in remeshing is to represent the surface signal using a compact 2D sample grid, since such a geometry image supports efficient storage, access, and processing.

Our first efforts focused on the cube domain, since its 6 faces can each be represented by a square geometry image. We were initially discouraged by the tetrahedron and octahedron domains, since their *isometric* unfoldings do not yield rectangles in the plane. (For example, such unfoldings are used for polyhedral maps in cartography [Furuti 1997].) However, we discovered that the *samples* of the regularly subdivided domain faces can be mapped 1-to-1 with samples of a 2D grid. As shown in Figure 5, the tetrahedron can be unfolded into a rectangle, and the octahedron into a square. Note that the unfolded tetrahedron wraps left-to-right, so its rightmost column in the geometry image is redundant. The 1-to-1 correspondence between domain samples and images samples is illustrated in Figure 6.

The remaining two Platonic solids would have more domain faces. The 20 triangles of the icosahedron could be unfolded to form 10 square geometry images or 5 rectangular ones. The dodecahedron seems impractical since its 12 pentagonal faces do not admit a regular sampling.

Since the samples in an image I really represent points on the domain D, filtering and reconstruction operations over the image must consider the domain geometry. Thus, for domains with triangle faces (tetrahedron and octahedron), this would imply linear as opposed to bilinear reconstruction.

Interestingly, in current graphics hardware, geometry is interpolated linearly (using the triangle primitive) whereas textures are interpolated bi-linearly (from 2D grids). Geometry images encourage us to consider unifying the reconstruction kernels. Thus, for tetrahedron and octahedron domains, both geometry and signals can be linearly interpolated (i.e. triangles with Gouraud-interpolated signal). And for the cube domain, both could be bi-linearly interpolated. From a signal-processing point-of-view, hexagonal grids (i.e. formed by equilateral triangles) actually offer better reconstruction characteristics than orthogonal grids for isotropic signals [Staunton 1999].

Figure 5: Cutting and unfolding the tetrahedron and octahedron. The colored edges represent the domain cuts.

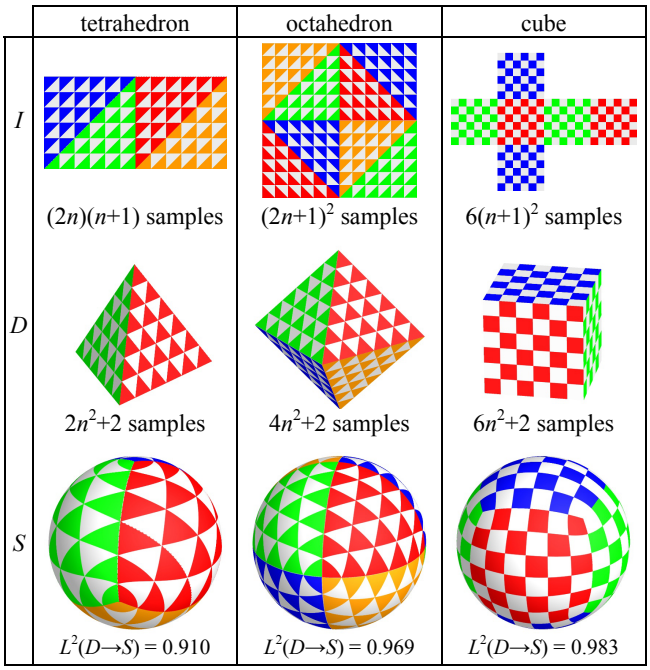

Figure 6: The three domains unfolded into geometry images, and mapped onto the sphere. (Samples lie at gridline intersections.)

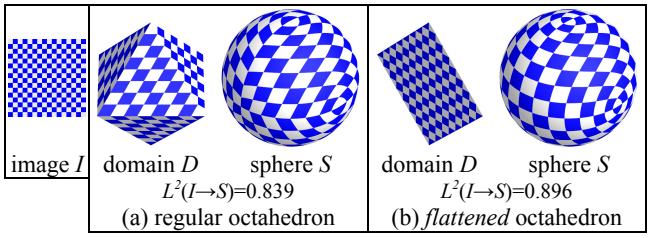

Figure 7: For a quadrilateral sampling, a flattened octahedron domain unfolds isometrically onto the square, yielding a smoother and more stretch-efficient parametrization.

Quadrilateral geometry image. If one desires a single geometry image with quadrilateral (bilinear) structure, the triangle-based octahedral parametrization produces a poor sampling because the non-isometric unfolding leads to derivative discontinuities on the domain edges (Figure 7a). As a better alternative, we construct a map from a *flattened* octahedron to the sphere. The flattened octahedron does unfold isometrically into a square, and still maintains the proper spherical topology. We tessellate the flattened octahedron and apply stretch-minimization as explained in the next section. We thus obtain a map that is smooth everywhere except at the 4 image boundary midpoints, and has improved stretch efficiency (see Figure 7b).

Boundary extension rules. Often, applications that process regular grids need to "hallucinate" samples that lie outside the grid boundaries. Traditional choices are to replicate the boundary values (i.e. clamping coordinates to the interior), to repeat the grid periodically, or to reflect the grid across its boundaries. These approaches correspond to the implied topologies of a disk (clamping both axes), a cylinder (periodicity along one axis), or a torus (periodicity along both axes).

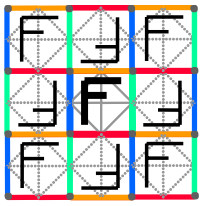

The boundary symmetries of our geometry images permit simple extension rules that allow continuous traversal over a spherical topology. The key is to extend the grid by rotating it 180° around the midpoints of boundaries. The inset figure shows this process applied to the octahedron, with the edges colored as in Figure 5. For the tetrahedron grid, we apply regular periodicity along the horizontal direction, and 180° rotations in the vertical direction.

These grid extension rules create an infinite lattice in 2D. Note that if one applies a separable, symmetric filter kernel to this lattice, the lattice symmetries are preserved. We make use of this property for image wavelet compression (Section 6).

4.2 Domain spherical parametrization (*D*•*S*)

The simplest parametrization from the domain to the sphere is a spherical projection, i.e. using a set of gnomonic maps. This is the traditional parametrization for environment cube-maps. However, as we saw in Figure 3, gnomonic projection creates high stretch distortion for large faces such as the domain faces.

Our solution is to apply our spherical parametrization optimization of Section 3 to an *n*-tessellated domain. Because here we seek to minimize stretch to the sphere instead of from the sphere, the stretch metric is measured in the direction $D \rightarrow S$ and is integrated over the sphere. (Stretch of this inverse map is easy to compute, since the Jacobian singular values are reciprocals of those in the forward map.)

The resulting stretch-optimized maps have excellent stretch efficiency, as shown in the bottom row of Figure 6. Moreover, the derivatives are visually continuous everywhere except at the domain vertices (which are not developable). For each domain, we pre-compute the map once at a high tessellation density and save it to disk. Then, we can sample this map for any requested density *n*. Figure 8 compares sampling the same model using all four domain types.

As an alternative, we also explored procedural maps using the spherical triangle maps presented in Section 3.2. For the cube, we split each cube face into 2, 4, or 8 triangles prior to the triangle mapping. As shown in Table 2, these procedural maps are less efficient than our optimized maps. Also, they generally lack derivative continuity across edges of the domain polyhedron.

	Stretch-optimiz.	Procedural Maps					
		Gnomonic	2-slerp	Arvo∘Turk^{-1}	Buss-Fillmore	Area	Subdiv.
tetra	**0.910**	0.628	0.871	0.846	**0.889**	0.849	0.645
octa	**0.969**	0.893	0.954	0.943	0.958	**0.958**	0.902
cube2	**0.983**	0.859	0.945	0.967	0.953	0.932	0.924
cube4		0.956	0.965	0.966	0.966	**0.978**	0.959
cube8		0.961	0.966	0.966	0.966	0.965	0.964
flat-octa	**0.896**	-	-	-	-	-	-

Table 2: L^2 stretch efficiencies for $D \rightarrow S$ using optimization and procedural maps. (Cube faces are split into 2, 4, or 8 triangles.)

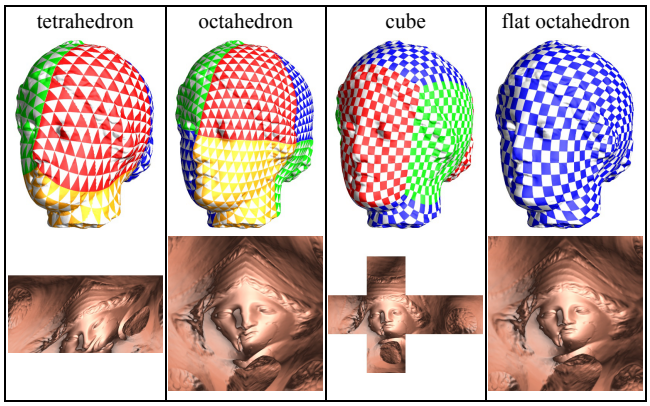

Figure 8: Remeshing using the four domain mappings.

5. Results and discussion

Our implementation consists of two modules. The first computes the surface spherical parametrization ($M \rightarrow S$). This is the slowest step in our pipeline, requiring about 7-25 minutes for our test models (25K-200K faces) on a 3GHz Pentium4 PC. The second module subdivides the domain *D* and maps these samples into both the geometry image ($D \rightarrow I$) and the sphere ($D \rightarrow S$). To efficiently map a point from the sphere back onto the surface, we locate the containing spherical triangle using a spatial data structure. By decomposing the parametrization into separate maps ($D \rightarrow S$ and $M \rightarrow S$), we avoid having to split the faces of the original mesh *M* along the edges of the polyhedral domain *D*.

Figure 9 shows a comparison of our remeshing scheme with that of Gu et al. [2002]. The Gu et al. parametrizations have more distortion at the cut path ends. Table 3 provides quantitative comparison of spherical parametrization and remeshing using our 3 domains and the square domain of Gu et al. Accuracy is measured as Peak Signal to Noise Ratio PSNR = 20 $\log_{10}(peak/d)$, where *peak* is the bounding box diagonal and *d* is the symmetric rms Hausdorff error (geometric distance) between the original mesh and the remesh. The tessellation number *n* is adjusted across domain types to approximately equalize sample sizes. The PSNR numbers indicate that our spherically parametrized geometry images have greater accuracy for sphere-like objects, as was to be expected. While the flexibility of the arbitrary cuts in Gu et al. is advantageous for some objects with long extremities (Figure 10), our results are close. The somewhat lower PSNR numbers for the cube-domain parametrizations are likely due to the heuristic selection of diagonals for triangulation.

Figure 10 shows an inherent limitation of spherical parametrization; for highly deformed shapes, one cannot simultaneously have both low stretch and conformality. Figure 11 shows the advantage of the stretch metric over the more traditional conformal metric, and also demonstrates the improvement due to our inverse-stretch regularization.

Figure 14 shows more examples using the 4 domain types. Note that all domains work well on any given model – we made no effort to select the domain per model. We prefer the octahedron domain for triangle-based (linear) reconstruction, and the flattened octahedron for quad-based (bilinear) reconstruction, because they each result in a single square geometry image. We explored the other two domains for research completeness.

The David in Figure 14 demonstrates a simple extension to our scheme that allows parametrization of surfaces with boundaries. Given an initial mesh with boundaries (holes), we triangulate each hole, marking the newly added faces with the attribute "hole". We apply our spherical parametrization algorithm to this closed

mesh, but we reduce the energy computed on all hole faces by a constant factor (e.g. 10^{-6}). The effect is that each hole is allowed to shrink in the parameter domain. However, it cannot collapse completely because the non-hole faces adjacent to the boundary do measure tangential stretch along the surface boundary. The precise 3D geometry of the hole faces is unimportant, since their sole purpose is effectively to prevent boundary self-intersection during optimization. During remeshing we ignore samples that lie in hole faces (colored in yellow).

	L^2 stretch efficiency $D \rightarrow M$				Remesh PSNR (dB)			
	tetra	octa	cube	[Gu]	tetra n=181	octa n=128	cube n=104	[Gu] n=256
Venus	0.864	0.943	0.937	0.706	82.3	83.4	81.8	80.7
bunny	0.673	0.706	0.703	0.639	79.6	79.8	79.0	78.2
David	0.767	0.828	0.822	0.644	67.8	68.0	68.2	68.2
gargoyle	0.568	0.643	0.656	0.669	78.1	79.2	78.2	77.0
armadillo	0.407	0.454	0.465	0.607	71.2	72.0	72.0	72.5
horse	0.349	0.363	0.389	0.351	76.6	76.9	76.6	74.3
cow	0.377	0.405	0.427	0.582	74.5	75.2	75.5	78.0
dinosaur	0.326	0.360	0.345	0.496	73.1	73.6	73.2	74.8

Table 3: Parametrization efficiencies and remesh accuracies.

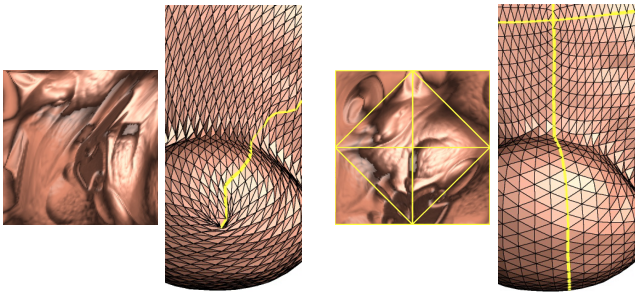

Gu et al. geometry image octahedron geometry image

Figure 9: Comparison of geometry images from Gu et al. [2002] and from our octahedron domain parametrization. The cut nodes in Gu et al. exhibit much more distortion.

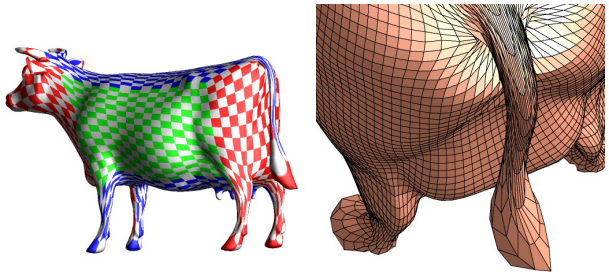

Figure 10: This cow model has a number of narrow extremities that make spherical parametrization challenging. Even at the tip of the tail, our method is robust and avoids undersampling. Of course, parametrization anisotropy along the tail becomes unavoidable, as evidenced by the thin remesh quadrilaterals.

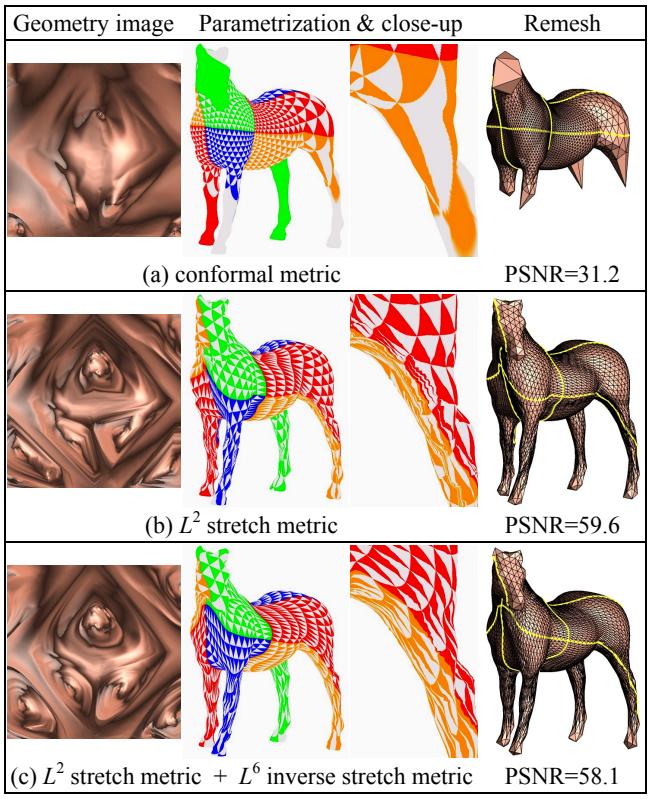

Figure 11: Parametrization comparison. (a) While the conformal metric better preserves angles, it leads to scale distortion and thus undersampling. (b) The stretch metric more uniformly distributes samples, but has irregular oversampling. (c) Our solution is to add a fraction of inverse stretch as a regularizing term.

6. Applications

Rendering. Our geometry images can be rendered as triangles by simply connecting the samples. For the tetrahedron and octahedron domains, the triangle connectivity is already provided. For the cube domain, we split each domain quad along the shorter diagonal, as in Gu et al. [2002].

Level-of-detail. If one selects the tessellation number n to be a power of 2, simpler models can be obtained easily by subsampling the geometry image. Gu et al. demonstrated this geometric subsampling, but the parametrization of their cut constrained the coarsest possible mesh, usually to n=32. In contrast, we can subsample all the way to n=1, obtaining coarse models with the connectivities of the domain polyhedra. Here are two examples:

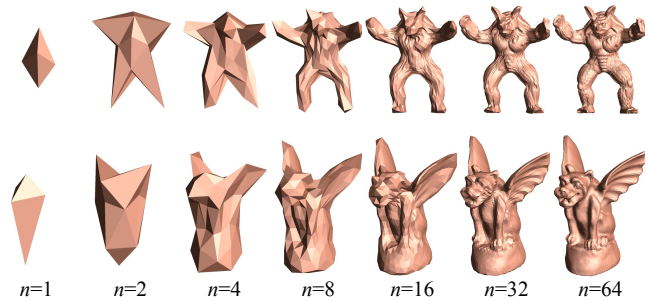

Morphing. Creating a morph between two models becomes easier once their spherical parametrizations are obtained. Any quaternion specifies a rigid alignment of the two sphere domains. Then, one can intersect the two spherical triangulations to form a mutual tessellation that can interpolate the models [Alexa 2000].

Our framework offers an alternative approach, which is to use spherical remeshing to create a *morphable geometry image*. We simply store two positions at each pixel of the geometry image, and interpolate between these points, as shown below.

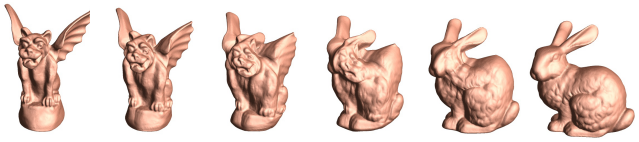

Note that the Gu et al. geometry images do not support such morphs, since their cut structures generally differ. Our geometry images can also morph between several models, or a whole space of models. In contrast, an approach based on mutual tessellation becomes impractical due to excessive mesh refinement.

To provide more control over the morph, it is common to let the user specify a set of k corresponding feature points on the models. The problem then becomes that of parametrization subject to constraints. Praun et al. [2001] present a technique involving a semi-regular domain. Alexa [2000] presents a warping scheme over the sphere, but the scheme does not always satisfy all constraints. Eckstein et al. [2001] present a robust planar solution, and perhaps their approach could be adapted to the sphere.

Compression. We have implemented two compression methods, one based on *spherical wavelets* [Schröder and Sweldens 1995], and the other on 2D *image wavelets* [Davis 1996]. Both methods work directly on the geometry images, with no explicit mesh data structures. Both make use of the boundary extension rules described in Section 4.1, and express high-pass detail in local tangential frames estimated from the low-pass surface. We follow each wavelet transform with quantization and entropy coding [Davis 1996], giving higher importance (3x) to the detail components normal to the surface [Khodakovsky et al. 2000]. We ran the Davis coder at various target bit rates to obtain the "spherical wavelet" and "image wavelet" data points in the rate-distortion graph of Figure 12.

For *spherical wavelets*, we use the geometry image from the octahedron domain and the lifted butterfly wavelet basis on the octahedron. As shown in Figure 12, our results are better than the compressed geometry images of Gu et al. [2002]. For small file sizes (≤3.5KB), our method also outperforms the coder of Khodakovsky et al. [Khodakovsky et al. 2000] on the bunny model, because our domain is simple and implicit.

For *image wavelet* coding, we use the geometry image defined with the flattened octahedron domain. One difficulty with using a standard image coder is that it is unaware of the boundary continuity conditions, and thus creates a lossy reconstructed surface with a gap along the domain cut. For this reason, the compression scheme of Gu et al. [2002] has to subsequently fuse the boundary using boundary topology stored in a sideband. This fusion results in sharp step functions that must then be diffused into the surface.

We are able to avoid this continuity issue altogether by modifying the image coder to use the boundary extension rules of Section 4.1, effectively working on an image with spherical topology. This modification only involves about 100 lines of code. We use symmetric image wavelet filters to preserve boundary symmetries at all image levels. During reconstruction we ensure proper duplication of the boundary values at all levels of the image pyramid, and as a result obtain a watertight mesh.

The extension rules effectively provide a smooth surface parametrization (i.e. continuous derivatives) except at four singular points, and this smoothness leads to significant compression improvements. As seen in Figure 12, for the bunny model the resulting PSNR curve consistently outperforms the specialized mesh coder of Khodakovsky et al. [2000]. Figure 13 shows the reconstructed remesh at various bit rates.

The elegance of our approach is that it uses ordinary image wavelets (no special-case bases) applied to a regular 2D grid data structure (no pointers).

Smooth subdivision. Losasso et al. [2003] adapt our spherical remeshing approach to construct smooth surfaces over geometry images. By exploiting the extension rules of our flattened octahedron parametrization, they represent a closed surface using a *single* bicubic B-spline patch. The surface is C^2 everywhere except at the four cut points where it is C^1. Representing the surface as a geometry image allows it to be subdivided in the fragment shader pipeline of currently available graphics hardware.

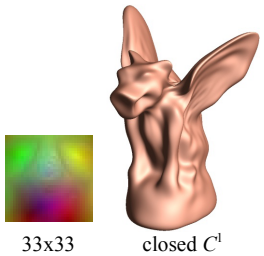

33x33 geom. image

closed C^1 surface

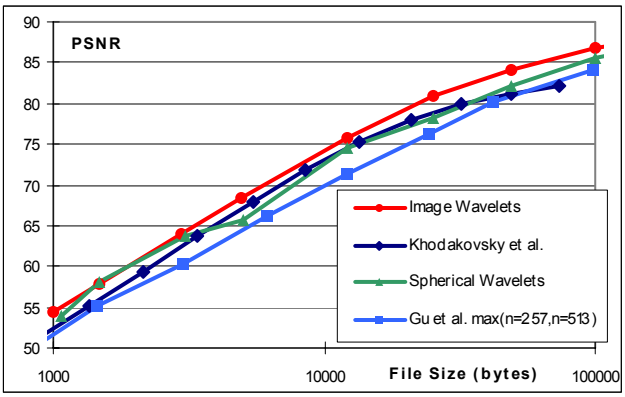

Figure 12: Rate distortion for different compression schemes applied to the bunny model. Both spherical and image wavelets are computed on a geometry image of size 513x513 (n=256).

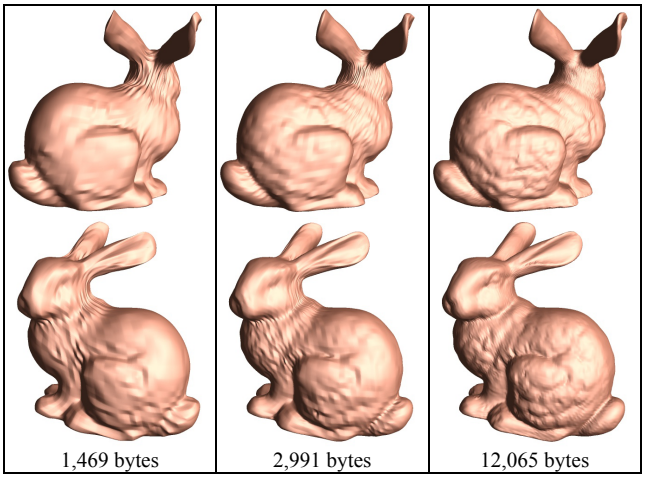

Figure 13: Geometry compression using image wavelets. (The four invisible domain cuts meet at the top of the rear right knee.)

7. Summary and future work

We have presented a robust algorithm for parametrizing genus-zero models onto the sphere, and introduced several approaches for resampling the spherical signal onto regular domains with simple boundary symmetries. We demonstrated our spherical parametrization framework on a collection of challenging models. The geometry images generated using our polyhedral samplings have simple structures that benefit a number of applications, including rendering, level-of-detail control, morphing, compression, and hardware evaluation of smooth surfaces.

There are a number of areas for future work:

- A more thorough investigation and comparison of compression approaches for spherically parametrized models.
- Treatment of the parametric singularities at the domain vertices, to allow more general signal-processing to be applied to the surfaces, such as general convolution.
- Use of fine-to-coarse integrated metric tensors to accelerate spherical parametrization and to enable signal-specialized parametrization as in Sander et al. [2002].
- Direct minimization of stretch across $D \rightarrow M$, to account for slight non-uniformity of $D \rightarrow S$ map, perhaps by modulating the stretch metric tensor during $S \rightarrow M$ optimization.
- Consistent spherical parametrizations among several models (i.e. with feature correspondences).

Acknowledgments

We thank the Digital Michelangelo Project at Stanford University for the David surface model.

References

ALEXA, M. 2000. Merging polyhedral shapes with scattered features. *The Visual Computer*, 16(1), pp. 26-37.

ALEXA, M. 2002. Recent advances in mesh morphing. *Computer Graphics Forum*, 21(2), pp. 173-196.

ARVO, J. 1995. Stratified sampling of spherical triangles. *ACM SIGGRAPH 95*, pp. 437-438.

BUSS, S., AND FILLMORE, J. 2001. Spherical averages and applications to spherical splines and interpolation. *ACM Transactions on Graphics*, 20(2), pp. 95-126.

CIGNONI, P., MONTANI, C., ROCCHINI, C., AND SCOPIGNO, R. 1998. A general method for recovering attribute values on simplified meshes. *IEEE Visualization 1998*, pp. 59-66.

COHEN, J., OLANO, M., AND MANOCHA, D. 1998. Appearance-preserving simplification. *ACM SIGGRAPH 98*, pp. 115-122.

DAVIS, G. 1996. Wavelet image compression construction kit. http://www.geoffdavis.net/dartmouth/wavelet/wavelet.html.

ECK, M., DEROSE, T., DUCHAMP, T., HOPPE, H., LOUNSBERY, M., AND STUETZLE, W. 1995. Multiresolution analysis of arbitrary meshes. *ACM SIGGRAPH 95*, pp. 173-182.

ECKSTEIN, I., SURAZHSKY, V., AND GOTSMAN, C. 2001. Texture mapping with hard constraints. *Eurographics 2001*, pp. 95-104.

FLOATER, M. 1997. Parametrization and smooth approximation of surface triangulations. *CAGD* 14(3), pp. 231-250.

FUNKHOUSER, T., MIN, P., KAZHDAN, M., CHEN, J., HALDERMAN, A., DOBKIN, D., AND JACOBS, D. 2003. A search engine for 3D models. *ACM Transactions on Graphics*, 22(1), January 2003, pp. 83-105.

FURUTI, C. 1997. http://www.progonos.com/furuti/.

GREENE, N. 1986. Environment mapping and other applications. *IEEE Computer Graphics and Applications*, 6(11).

GRIMM, C. 2002. Simple manifolds for surface modeling and parametrization. *Shape Modeling International 2002*.

GU, X., GORTLER, S., AND HOPPE, H. 2002. Geometry images. *ACM SIGGRAPH 2002*, pp. 355-361.

GOTSMAN, C., GU, X., AND SHEFFER, A. 2003. Fundamentals of spherical parameterization for 3D meshes. *ACM SIGGRAPH 2003*.

GUSKOV, I., VIDIMČE, K., SWELDENS, W., AND SCHRÖDER, P. 2000. Normal meshes. *ACM SIGGRAPH 2000*, pp. 95-102.

HAKER, S., ANGENENT, S., TANNENBAUM, S., KIKINIS, R., SAPIRO, G., AND HALLE, M. 2000. Conformal surface parametrization for texture mapping. *IEEE TVCG*, 6(2), pp. 181-189.

HOPPE, H. 1996. Progressive meshes. *ACM SIGGRAPH 96*, pp. 99-108.

HORMANN, K., GREINER, G., AND CAMPAGNA, S. 1999. Hierarchical parametrization of triangulated surfaces. *Vision, Modeling, and Visualization 1999*, pp. 219-226.

KENT, J., CARLSON, W., AND PARENT, R. 1992. Shape transformation for polyhedral objects. *ACM SIGGRAPH 92*, pp. 47-54.

KHODAKOVSKY, A., SCHRÖDER, P., AND SWELDENS, W. 2000. Progressive geometry compression. *ACM SIGGRAPH 2000*, 271-278.

KOBBELT, L., VORSATZ, J., LABSIK, U., AND SEIDEL, H.-P. 1999. A shrink wrapping approach to remeshing polygonal surfaces. *Eurographics 1999*, pp. 119-130.

LEE, A., SWELDENS, W., SCHRÖDER, P., COWSAR, L., AND DOBKIN, D. 1998. MAPS: Multiresolution adaptive parametrization of surfaces. *ACM SIGGRAPH 98*, pp. 95-104.

LEE, A., MORETON, H., AND HOPPE, H. 2000. Displaced subdivision surfaces. *ACM SIGGRAPH 2000*, pp. 85-94.

LÉVY, B., PETITJEAN, S., RAY, N., AND MAILLOT, J. 2002. Least squares conformal maps for automatic texture atlas generation. *ACM SIGGRAPH 2002*, pp. 362-371.

LOSASSO, F., HOPPE, H., SCHAEFER, S., AND WARREN, J. 2003. Smooth geometry images. Submitted for publication.

MAILLOT, J., YAHIA, H., AND VERROUST, A. 1993. Interactive texture mapping. *ACM SIGGRAPH 93*, pp. 27-34.

PRAUN, E., SWELDENS, W., AND SCHRÖDER, P. 2001. Consistent mesh parametrizations. *ACM SIGGRAPH 2001*, pp. 179-184.

QUICKEN, M., BRECHBÜHLER, C., HUG, J., BLATTMANN, H., SZÉKELY, G. 2000. Parametrization of closed surfaces for parametric surface description, *CVPR 2000*, pp. 354-360.

SANDER, P., SNYDER, J., GORTLER, S., AND HOPPE, H. 2001. Texture mapping progressive meshes. *ACM SIGGRAPH 2001*, pp. 409-416.

SANDER, P., GORTLER, S., SNYDER, J., AND HOPPE, H. 2002. Signal-specialized parametrization. *Eurographics Workshop on Rendering 2002*, pp. 87-100.

SCHRÖDER, P. AND SWELDENS, W. 1995. Spherical wavelets: Efficiently representing functions on the sphere. *ACM SIGGRAPH 95*, 161-172.

SHAPIRO, A. AND TAL, A. 1998. Polygon realization for shape transformation. *The Visual Computer*, 14 (8-9), pp. 429-444.

SHEFFER, A., GOTSMAN, C., AND DYN, N. 2003. Robust spherical parameterization of triangular meshes. 4th Israel-Korea Bi-National Conf. on Geometric Modeling and Computer Graphics, pp. 94-99.

SHEFFER, A., AND HART, J. 2002. Seamster: Inconspicuous low-distortion texture seam layout. *IEEE Visualization 2002*, pp. 291-298.

SORKINE, O., COHEN-OR, D., GOLDENTHAL, R., AND LISCHINSKI, D. 2002. Bounded-distortion piecewise mesh parametrization. *IEEE Visualization 2002*.

STAUNTON, R. 1999. Hexagonal sampling in image processing. In *Advances in imaging and electron physics*, Vol. 107, Academic Press.

TURK, G. 1990. Generating random points in triangles. *Graphics Gems*, Academic Press, pp. 649-650.

TODHUNTER, I., AND LEATHEM, J.G. 1949. *Spherical Trigonometry*, Macmillan and Co, Limited.

WOOD, Z., DESBRUN, M., SCHRÖDER, P., AND BREEN, D. 2000. Semi-regular mesh extraction from volumes. *IEEE Visualization 2000*, pp. 275-282.

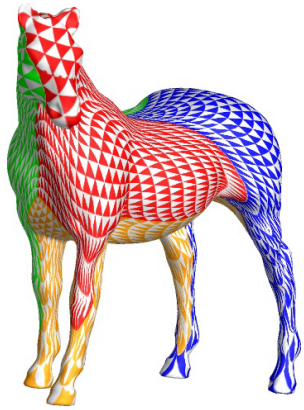
tetrahedron parametrization

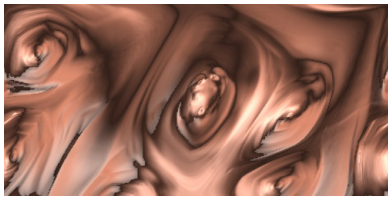
geometry image (362x182)

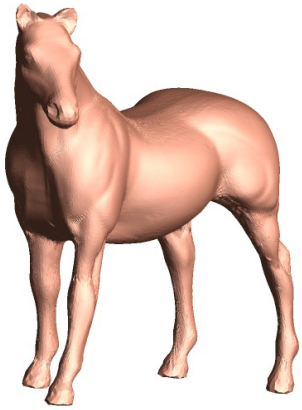
flat-shaded remesh (65,524 unique vertices)

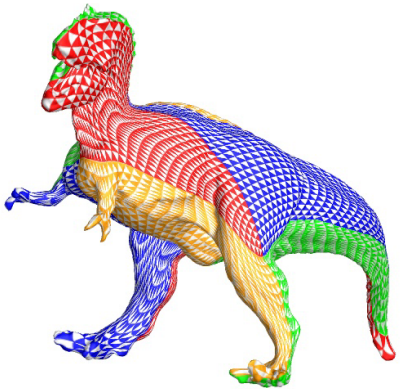
octahedron parametrization

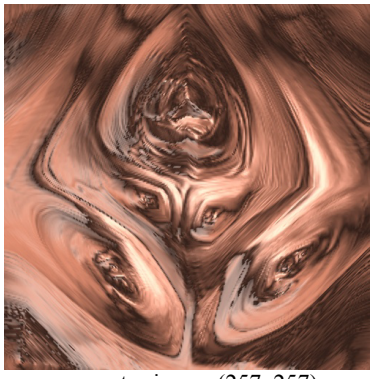
geometry image (257x257)

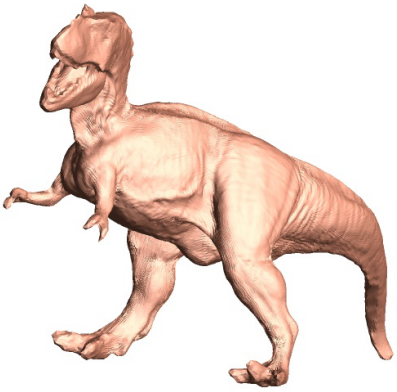
flat-shaded remesh (65,538 unique vertices)

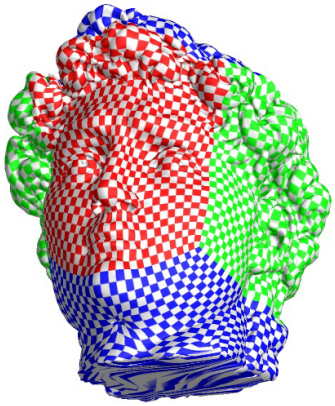
cube parametrization


geometry image (6x105x105)


flat-shaded remesh (64,523 non-hole vertices)

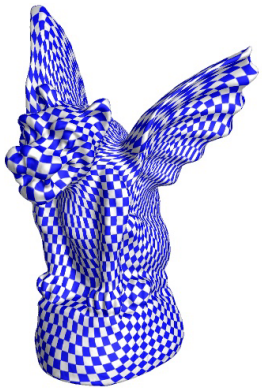
flat octahedron parametrization

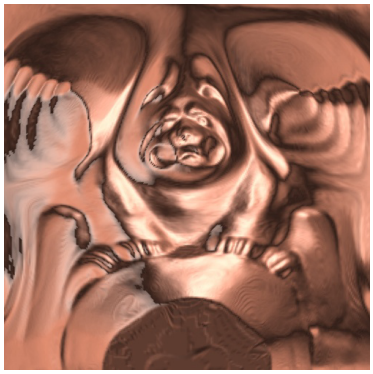
geometry image (257x257)


flat-shaded remesh (65,538 unique vertices)

Figure 14: Results of spherical parametrization and remeshing using all four domain types. For visualization, the geometry images in the middle column are shown shaded using two antipodal lights. (Shading is based solely on the remesh – there are no stored normals.)